Biological and physical controls on N_2, O_2, and CO_2 distributions in contrasting Southern Ocean surface waters

Philippe D. Tortell[1,2], Henry C. Bittig[3], Arne Körtzinger[3], Elizabeth M. Jones[4], and Mario Hoppema[4]

[1]Department of Earth, Ocean and Atmospheric Sciences, University of British Columbia, Vancouver, British Columbia, Canada, [2]Department of Botany, University of British Columbia, Vancouver, British Columbia, Canada, [3]Marine Biogeochemistry, GEOMAR Helmholtz Centre for Ocean Research Kiel, Kiel, Germany, [4]Alfred Wegener Institute, Helmholtz Centre for Polar and Marine Research, Bremerhaven, Germany

Abstract We present measurements of pCO_2, O_2 concentration, biological oxygen saturation ($\Delta O_2/Ar$), and N_2 saturation (ΔN_2) in Southern Ocean surface waters during austral summer, 2010–2011. Phytoplankton biomass varied strongly across distinct hydrographic zones, with high chlorophyll a (Chl a) concentrations in regions of frontal mixing and sea ice melt. pCO_2 and $\Delta O_2/Ar$ exhibited large spatial gradients (range 90 to 450 μatm and −10 to 60%, respectively) and covaried strongly with Chl a. However, the ratio of biological O_2 accumulation to dissolved inorganic carbon (DIC) drawdown was significantly lower than expected from photosynthetic stoichiometry, reflecting the differential time scales of O_2 and CO_2 air-sea equilibration. We measured significant oceanic CO_2 uptake, with a mean air-sea flux ($\sim -10 \, mmol \, m^{-2} \, d^{-1}$) that significantly exceeded regional climatological values. N_2 was mostly supersaturated in surface waters (mean ΔN_2 of +2.5%), while physical processes resulted in both supersaturation and undersaturation of mixed layer O_2 (mean $\Delta O_{2phys} = 2.1\%$). Box model calculations were able to reproduce much of the spatial variability of ΔN_2 and ΔO_{2phys} along the cruise track, demonstrating significant effects of air-sea exchange processes (e.g., atmospheric pressure changes and bubble injection) and mixed layer entrainment on surface gas disequilibria. Net community production (NCP) derived from entrainment-corrected surface $\Delta O_2/Ar$ data, ranged from ~ -40 to $> 300 \, mmol \, O_2 \, m^{-2} \, d^{-1}$ and showed good coherence with independent NCP estimates based on seasonal mixed layer DIC deficits. Elevated NCP was observed in hydrographic frontal zones and stratified regions of sea ice melt, reflecting physical controls on surface water light fields and nutrient availability.

1. Introduction

The Southern Ocean plays a key role in global nutrient and carbon cycles [*Sarmiento et al.*, 2004; *Schlitzer*, 2002]. This vast region contributes significantly to oceanic CO_2 uptake through the vertical export of particulate organic carbon [*Honjo et al.*, 2008; *Schlitzer*, 2002; *Trull et al.*, 2001] and the subduction of CO_2-rich polar water masses into the ocean interior [*Caldeira and Duffy*, 2000; *Sarmiento and Toggweiler*, 1984]. These biological and physical carbon pumps also transport oxygen and macronutrients into the low latitudes, where they influence biological productivity over large spatial scales [*Marinov et al.*, 2006; *Sarmiento et al.*, 2004]. In the offshore pelagic realm, Southern Ocean primary production and biological CO_2 uptake appear to be controlled by a combination of light and iron limitation [*Boyd*, 2002]. Large-scale patterns of aeolian iron deposition have been linked to spatial gradients in surface water productivity [*Cassar et al.*, 2007], while vertical mixing at frontal zones has been shown to drive mesoscale and submesoscale biological gradients [*Sokolov and Rintoul*, 2007]. Relative to the open ocean, field data are sparse over much of the Antarctic continental shelf and marginal ice zone (MIZ), where productivity is influenced by iron input from sediments [*Coale et al.*, 2005; *Planquette et al.*, 2013] and melting ice [*Gerringa et al.*, 2012; *Sedwick and DiTullio*, 1997] and by large seasonal cycles in solar irradiance, mixed layer depth, and sea ice cover [*Arrigo and van Dijken*, 2003]. Although these high-latitude regions contribute disproportionately (on an areal basis) to Southern Ocean nutrient and carbon cycles [*Arrigo et al.*, 2008], their biological and physical dynamics remain poorly described.

Here we present new results from a 2 month survey of surface hydrography and dissolved gas concentrations across the Atlantic sector of the Southern Ocean and the region west of the Antarctic Peninsula. We use our

observations to characterize the spatial variability of surface gases in contrasting Southern Ocean regions (offshore pelagic, continental shelf, and MIZ) and to examine the relative influence of physical versus biological controls on biogeochemical processes. The interplay of physical and biological forcing is particularly important in determining surface water pCO_2 and O_2 distributions. Net community production (NCP, i.e., gross photosynthesis minus community respiration) leads to CO_2 drawdown (i.e., decreased pCO_2) in the mixed layer, coupled with biologically induced O_2 supersaturation [*Carrillo et al.*, 2004]. NCP is sensitive to physical factors (e.g., wind speed, solar irradiance, and ice cover) that control nutrient supply and mixed layer light intensity. Physical processes also influence surface O_2 and CO_2 by modulating the strength of diffusive air-sea exchange, which acts to restore gas concentrations back to atmospheric equilibrium, and bubble processes, which lead to supersaturation of surface water gases [*Keeling*, 1993]. Due to chemical buffering of the inorganic C system in seawater, the diffusive air-sea equilibration time scale is typically approximately tenfold slower for CO_2 than for O_2 [*Sarmiento and Gruber*, 2006], and gas exchange can thus overprint the biological production signal, shifting the pCO_2-O_2 relationship away from photosynthetic stoichiometry [*Kortzinger et al.*, 2008].

Changes in surface water temperature and salinity can also influence O_2 and CO_2 distributions through their effect on gas solubility. For O_2, these thermodynamic effects can be removed by normalization to argon, a biologically inert gas with solubility properties that are virtually identical to O_2. The O_2/Ar ratio thus serves as a specific tracer for biological O_2 cycling [*Craig and Hayward*, 1987], and recent field measurements of O_2/Ar disequilibrium (ΔO_2/Ar) have been used to map the large-scale spatial distribution of NCP in Southern Ocean surface waters [*Cassar et al.*, 2011; *Castro-Morales et al.*, 2013; *Reuer et al.*, 2007; *Shadwick et al.*, 2014; *Tortell and Long*, 2009]. NCP estimates derived from ΔO_2/Ar measurements are based on a steady state mixed layer model [*Kaiser et al.*, 2005; *Reuer et al.*, 2007], where vertical and lateral exchange of O_2 into the mixed layer is assumed to be negligible and NCP can thus be equated to the biologically induced sea-air flux of O_2 (O_2 bioflux). These assumptions are likely invalid over significant portions of the Southern Ocean, where vertical entrainment of biologically modified subsurface waters leads to significant uncertainty in derived mixed layer NCP values [*Jonsson et al.*, 2013]. Better constraints on the physical contributions to mixed layer O_2 mass balance are thus needed to improve the use of ΔO_2/Ar as a productivity tracer.

Like Ar, N_2 is biologically inert in the Southern Ocean, where nitrogen fixation and denitrification are inhibited by high NO_3^- and O_2 concentrations, respectively. Given the high atmospheric concentrations of N_2 and its relatively low solubility in seawater, this gas provides a useful tracer for air-sea exchange processes, including bubble injection [*Schudlich and Emerson*, 1996]. A number of studies have used surface ocean N_2 disequilibrium measurements (ΔN_2) to examine air-sea exchange [*Emerson et al.*, 2002; *Hamme and Emerson*, 2006; *Vagle et al.*, 2010], and a mechanistic framework has recently been developed to quantitatively interpret surface N_2 data [*Liang et al.*, 2013; *Nicholson et al.*, 2008, 2011; *Stanley et al.*, 2009]. At present, we are aware of only one published ΔN_2 data set from Southern Ocean waters [*Weeding and Trull*, 2014]. Additional ΔN_2 measurements from this region are thus needed to validate the model-based calculations under conditions of high wind speeds, strong gradients in atmospheric pressure and significant bubble injection fluxes.

Using simultaneous measurements of N_2, O_2, ΔO_2/Ar, and CO_2, in combination with ancillary data and box model calculations, we examined the dominant controls on surface gas saturation states in contrasting Southern Ocean surface waters. Our results provide insight into the factors driving gas dynamics in various subregions of the Southern Ocean, demonstrating clear regional differences in the relative importance of physical and biological forcing. Our observations reveal strong biological controls on surface CO_2 and O_2 distributions, with a significant imprint of air-sea exchange. Using box model calculations, we show that the formulation of *Nicholson et al.* [2011] is able to provide reasonable estimates of physically induced changes in O_2 and N_2 saturation states, and we derive NCP estimates that are corrected for entrainment of biologically modified subsurface waters into the mixed layer. Our work builds on the recent studies of *Shadwick et al.* [2014] examining CO_2, O_2, and ΔO_2/Ar along a transect south of Australia and *Weeding and Trull* [2014], who present a mooring-based O_2 and N_2 time series for the Sub-Antarctic region south of Tasmania. To our knowledge, our work represents the first simultaneous measurements of pCO_2, ΔO_2, ΔO_2/Ar, and ΔN_2 for the Southern Ocean, and we show how these combined observations can provide powerful insights into surface water biogeochemical processes across a range of hydrographic regimes.
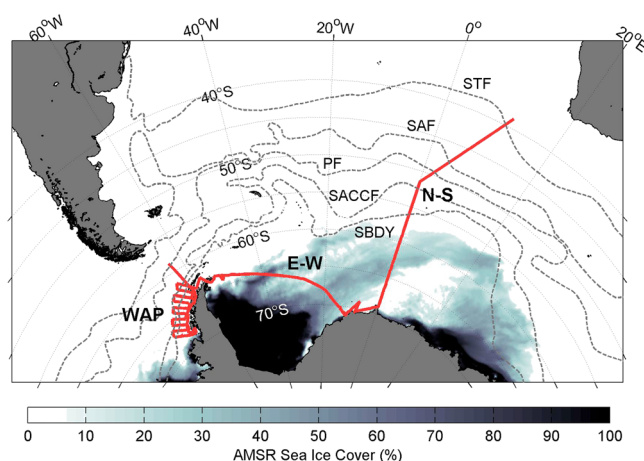
Figure 1. Map of the sampling area showing the cruise track (solid red line) and the position of various hydrographic fronts (dotted lines). From north to south, the fronts are Subtropical Front (STF), Sub-Antarctic Front (SAF), Polar Front (PF), Southern Antarctic Circumpolar Current Front (SACCF), and Southern Boundary of the Antarctic Circumpolar Current (SBdy). The location of mean frontal positions was derived from *Orsi et al.* [1995]. N-S, E-W, and WAP denote different portions of our sampling region, as described in the text. Grey/black shading around the Antarctic continent represents the mean sea ice cover during the period of our survey, derived from the Advanced Microwave Scanning Radiometer–EOS (AMSR-E) satellite product.

2. Methods

2.1. Study Site and Hydrographic Measurements

We conducted a 10 week survey of Southern Ocean waters from 29 November 2010 to 3 February 2011 on board the research vessel *Polarstern* (cruise ANT-XXVII/2; [*Rohardt et al.*, 2011]). Our cruise track from Cape Town, South Africa, to Punta Arenas, Chile (Figure 1), encompassed a number of distinct hydrographic regimes. For the purposes of our analysis, we separate the cruise track into three subregions. We first sampled a N-S transect ~40°S to 70°S, crossing a number of prominent hydrographic fronts [*Orsi et al.*, 1995], including the Subtropical Front (STF), Sub-Antarctic Front (SAF), Polar Front (PF), Southern Antarctic Circumpolar Current Front (SACCF), and Southern Boundary of the Antarctic Circumpolar Current (SBdy). We then followed an E-W transect along the outer edge of the Weddell Sea MIZ and conducted an intensive survey of the West Antarctic Peninsula (WAP) along the Palmer Long Term Ecological Research (LTER) sampling grid [*Waters and Smith*, 1992].

Sea surface temperature (SST) and salinity (SSS) were measured continuously along the cruise track using an onboard thermosalinograph (TSG; Sea-Bird Electronics, model SBE-21) sampling from an uncontaminated seawater supply with a nominal intake depth of 11 m. Daily calibrations of the TSG salinity measurements were conducted using discrete samples analyzed on a salinometer (Optimare GmbH, Precision Salinometer). Sea surface Chl *a* fluorescence, used as a proxy for bulk phytoplankton biomass, was continuously measured by the ship's underway fluorometer (WET labs, ECO). The fluorometer data were not calibrated to absolute Chl *a* concentrations and are thus used here only as a relative measure of total phytoplankton abundance. Some daytime nonphotochemical quenching of Chl *a* fluorescence is expected, independent of changes in phytoplankton biomass.

Depth profiles of seawater potential temperature, salinity, and Chl *a* fluorescence were obtained from conductivity-temperature-depth (CTD) casts at 188 stations along the cruise track. Temperature and conductivity were measured with Sea-Bird SBE3plus and SBE4 sensors, respectively, while Chl *a* fluorescence was measured with a WET labs ECO fluorometer. Temperature and salinity profiles were used to define the mixed layer depth for each station based on the curvature of near-surface layer density or temperature profiles as described by *Lorbacher et al.* [2006]. Mixed layer temperature and salinity data derived from CTD casts showed very good agreement with surface TSG data (mean offset of −0.078°C and −0.01, respectively). The concentration of O_2 in depth profiles was measured using a CTD-mounted Sea-Bird SBE43 sensor. The CTD O_2 sensor was calibrated using Winkler titrations of discrete samples, with visual endpoint determination using a starch indicator (precision of 0.3 μmol L^{-1}) and KIO$_3$ standardization of the thiosulfate titration solutions [*Dickson*, 1994]. All of the CTD sensors were sent to the manufacturer for calibration prior to and immediately after the cruise. Full quality-controlled hydrographic data from the cruise are available in the Pangaea database (www.pangaea.de).

2.2. Surface Water Gas Measurements

Surface pCO_2 and O_2/Ar ratios were measured every ~30 s from the keel intake supply using membrane inlet mass spectrometry (MIMS), following the protocols described by *Tortell et al.* [2011]. At typical cruising speeds of ~15−20 km h^{-1}, this sampling frequency translates into one measurement every ~200 m along the cruise

track. The pCO_2 measurements were calibrated using temperature-controlled seawater standards [*Tortell et al.*, 2011], and the resulting pCO_2 data were corrected to in situ SST following [*Takahashi et al.*, 2002]. Note that pCO_2 data are not available for much of the N-S transect due to instrument problems. O_2/Ar measurements in the flow-through seawater, $(O_2/Ar)_{meas}$, were normalized to values measured every few hours in air-equilibrated, temperature-controlled seawater standards, $(O_2/Ar)_{sat.}$ [*Tortell et al.*, 2011], to derive a biological O_2 saturation term, $\Delta O_2/Ar$, expressed in % deviation from equilibrium.

This term was calculated as [*Craig and Hayward*, 1987]

$$\Delta O_2/Ar = \left[(O_2/Ar)_{meas}/(O_2/Ar)_{sat} - 1\right] \times 100 \qquad (1)$$

Surface O_2 concentration measurements were made using an optode (Aanderaa Data Instruments, model 3830), while total gas pressure (mbar) was measured using a gas tension device (Pro-Oceanus, model HGTD). The gas tension device was not functional during the latter half of the cruise. Both the optode and HGTD were submerged in a thermally insulated flow-through box connected to the keel seawater intake supply and set to acquire data with a 1 min resolution (close to the response time of the HGTD). The optode O_2 measurements were calibrated against CTD-O_2 data and cross validated against discrete Winkler titrations. The O_2 saturation state (ΔO_2; % deviation from equilibrium) was derived from measured O_2 concentrations and an equilibrium O_2 concentration computed from surface water temperature, salinity, and atmospheric pressure with the solubility function of *Garcia and Gordon* [1992]. Using our optode and MIMS data, we derived an estimate of the physical contribution to O_2 disequilibria in surface waters, ΔO_{2phys}.

$$\Delta O_{2phys} = \Delta O_{2optode} - \Delta O_2/Ar_{MIMS} \qquad (2)$$

The rationale for this approach is that optode-based ΔO_2 is sensitive to both physical and biological influences, whereas MIMS-based $\Delta O_2/Ar$ reflects only the biological contribution to O_2 disequilibria [*Craig and Hayward*, 1987], after normalizing for physical effects using the biologically inert analog, argon. As calculated here (2), ΔO_{2phys} is thus functionally equivalent to the physically induced changes in Argon saturation, ΔAr.

Following the approach of *McNeil et al.* [2005, 1995], we derived estimates of N_2 partial pressure from GTD total gas pressure by subtracting the partial pressures of O_2 (derived from optode measurements), water vapor (calculated from SST and SSS), and Ar.

$$pN_2 \approx pTotal - pO_2 - pH_2O - pAr \qquad (3)$$

In previous studies, seawater Ar concentrations have been assumed to be at atmospheric equilibrium values. This assumption contributes only a small uncertainty ($<0.1\%$) to the calculation of N_2 concentrations [*McNeil et al.*, 1995], since Ar is a minor constituent of total partial pressure and varies by only a few percent. Indeed, we observed a negligible difference between pN_2 calculated assuming 100% Ar saturation and calculations that included a specific ΔAr term (derived from ΔO_{2phys}). Similarly, the inclusion of pCO_2 into the calculation did not have a significant effect on the resulting pN_2. The N_2 saturation state (ΔN_2) was calculated from GTD-derived N_2 concentrations and observed atmospheric pressure using the SST and salinity-dependent N_2 solubility constant of *Hamme and Emerson* [2004].

2.3. Ancillary Data

Ancillary meteorological and oceanographic data from a number of sources were used to provide a broader environmental context for our observations, and input data for model calculations (see below). Instantaneous measurements of sea level atmospheric pressure, wind speed (corrected to 10 m above sea level), and solar irradiance were obtained from weather station sensors on board the research vessel. Additional synoptic data on wind speed, sea level atmospheric pressure, and humidity were obtained from the National Centers for Environmental Prediction (NCEP) reanalysis (http://www.esrl.noaa.gov/psd/data/reanalysis/reanalysis.shtml) at 2.5° and 6 h resolution, while regional SST information was derived from NOAA Optimum Interpolation Sea Surface Temperature (OISST) (http://www.ncdc.noaa.gov/sst/) at 0.25° and 24 h resolution. The NCEP wind speed data showed reasonably good agreement with the instantaneous shipboard measurements ($r = 0.78$, root-mean-square error $= 2.9\,m\,s^{-1}$). Although there was a slight offset toward lower wind speeds in the NCEP data, the mean difference ($-0.94\,m\,s^{-1} \pm 3.11$) was not significantly different from zero. Sea

ice data (% cover) at 3 km and 24 h resolution were derived from AMSR-E satellite imagery using the ARTIST Sea Ice (ASI) reprocessing algorithm provided by the Institute of Environmental Physics at the University of Bremen, Germany [*Spreen et al.*, 2008]. Regional sea surface salinity was obtained from the Mercator global operational system PSY3V3 model at 0.25° and 24 h resolution (http://www.mercator-ocean.fr/eng/produits-services/Reference-products#tps_differe). Surface Chl *a* concentrations were obtained from Level 3 AquaModis satellite data (http://oceancolor.gsfc.nasa.gov/cgi/l3). We used 9 km resolution imagery, with 8 day composite data linearly interpolated to daily values.

2.4. CO_2 Flux Calculations

Surface gas measurements and wind speed data were used to derive sea-air flux estimates for CO_2. The CO_2 fluxes were calculated as

$$F_{CO_2} = k_{CO_2} \, \alpha_{CO_2} \, (pCO_{2sw} - pCO_{2atm}) \, (1-A)^{0.4} \tag{4}$$

where k_{CO_2} is the gas transfer velocity ($m \, d^{-1}$), calculated from wind speed data and the temperature-dependent Schmidt number using the parameterization of *Sweeney et al.* [2007], α_{CO_2} is the temperature and salinity-dependent solubility of CO_2 [*Weiss*, 1974], and A is the fraction of sea surface covered by ice. The exponential term used to scale gas exchange as a function of ice cover is derived from *Loose et al.* [2009]. For these flux calculations, we used an atmospheric CO_2 mole fraction of 396 ppmv, derived from the GlobalView pCO_2 data (www.esrl.noaa.gov/gmd/ccgg/globalview/; 60°S to 70°S, December 2010 to February 2011), corrected to 100% humidity at SST and SSS and the atmospheric pressure derived from ship-based sensors. Wind speeds used for the flux calculations were derived from 1 week averages of the NCEP reanalysis product, matched to the ship's position along the cruise track.

2.5. Carbonate System Measurements and Calculations

Discrete samples for carbonate system measurements were collected at selected stations along the cruise track using 12 L Niskin bottles mounted on the CTD rosette. Total alkalinity was measured using potentiometric gran titration [*Brewer et al.*, 1986], calibrated against certified reference material (batches 100 and 105) supplied by Doctor Andrew Dickson, Scripps Institution of Oceanography [*Dickson et al.*, 2007]. The precision of the alkalinity measurements was $1.5 \, \mu mol \, kg^{-1}$. Seawater (500 mL) for dissolved inorganic carbon (DIC) analysis was collected in borosilicate glass bottles and analyzed within 20 h using a VINDTA 3C instrument (Versatile INstrument for the Determination of Total Alkalinity, Marianda, Kiel). The DIC concentration was determined by coulometric analysis [*Johnson et al.*, 1987], with calibration against certified reference materials (CRM, batches 100 and 105) performed at the start and end of each measurement cycle. The precision of the DIC measurements was $1.0 \, \mu mol \, kg^{-1}$, based on the average difference between all CRM in-bottle duplicate analyses ($n = 87$), and the accuracy was estimated as $2.0 \, \mu mol \, kg^{-1}$.

Depth-integrated DIC deficits were calculated from vertical profiles relative to the concentration at the depth of the potential temperature minimum, representing the Winter Water. The depth of the potential temperature minimum was determined from the CTD profiles. Vertical integration to the potential temperature minimum was used to derive the chemical deficits in the summer surface layer. DIC data were normalized to average Winter Water salinity (34.2, $n = 105$) to account for dilution through addition of sea ice meltwater. The chemical deficits, calculated in this way, represent the time-integrated change of the surface ocean since the end of the winter. This technique assumes that DIC concentrations at the potential temperature minimum represent the winter reference with no significant lateral or vertical exchange. This assumption has been used in prior studies [*Hoppema et al.*, 2007; *Jennings et al.*, 1984; *Rubin et al.*, 1998] and appears to be reasonably robust for the Weddell Sea [*Hoppema et al.*, 2000b].

In order to obtain high spatial resolution surface carbonate system data along the cruise track, we derived an empirical linear relationship between salinity and alkalinity along the E-W and WAP transects ($n = 2098$, $r^2 > 0.85$, root-mean-square error = $6.1 \, \mu mol \, kg^{-1}$) and used this relationship to compute alkalinity from thermosalinograph salinity measurements. Total dissolved inorganic carbon (DIC) along the cruise track was then computed from measured pCO_2 and the derived alkalinity using CO2SYS [*Pierrot et al.*, 2006], with the equilibrium constants of *Mehrbach et al.* [1973] refit by *Dickson and Millero* [1987]. For the WAP and Weddell regions, the root-mean-square error of the DIC estimates derived from this analysis was 7.1

and $3.8 \, \mu mol \, kg^{-1}$, respectively. This error term was based on a comparison of DIC values obtained using measured versus empirically derived alkalinity.

2.6. Box Model Calculations

Following the work of *Emerson et al.* [2008] and *Nicholson et al.* [2011], we used a simple box model to assess the physical contributions to N_2 and O_2 disequilibria in the mixed layer. The 1-D model includes an air-sea gas exchange term, F_{as}, and a subsurface water entrainment term, F_{entr}, associated with mixed layer deepening events. Lateral and vertical advection and vertical diffusive mixing were assumed to be negligible, and no biological production/consumption term was included in order to isolate physical forcing. For a given gas, x, the change in mixed layer concentrations, dc_x, was computed as

$$mld \, dc_x/dt = F_{as,x} + F_{entr,x} \tag{5}$$

where mld is mixed layer depth. The air-sea flux term, F_{as}, was separated into several components; diffusive gas exchange, F_{dif}, injection of small bubbles, F_{inj}, and air-water interface exchange across larger bubble surfaces, F_{ex}. These gas exchange terms were all scaled to the fraction of open water, A, following *Loose et al.* [2009], as described in section 2.4. The total air-sea flux term (F_{as}) for gas x was thus computed as

$$F_{as,x} = \left(F_{dif,x} + F_{inj,x} + F_{ex,x} \right) (1 - A)^{0.4} \tag{6}$$

$$F_{dif,x} = -k_x(c_x - \alpha_x p_x) \tag{7}$$

$$F_{inj,x} = A_{inj} \, p_x (u_{10} - 2.27)^3 \tag{8}$$

$$F_{ex,x} = A_{ex} \, p_x \left(D_x / 1 \, m^2 s^{-1} \right)^{0.5} \left(\alpha_x / 1 \, mol \, m^{-3} atm^{-1} \right) (u_{10} - 2.27)^3 \tag{9}$$

where k_x is the gas transfer velocity ($m \, s^{-1}$) calculated following *Sweeney et al.* [2007], α_x the solubility ($mol \, m^{-3} \, atm^{-1}$), p_x the partial pressure calculated from the mole fraction in dry air and the dry atmospheric pressure ($p_x = \chi_x \, p_{atm,dry}$), and D_x the diffusion coefficient ($m^2 \, s^{-1}$). The injection and exchange rates A_{inj} and A_{ex} ($mol \, s^2 \, m^{-5} \, atm^{-1}$) given in *Nicholson et al.* [2011] were derived for average wind speeds. For our calculations based on short-term wind speeds, we use a flux enhancement factor, R, of 1.5 as discussed in *Nicholson et al.* [2011]. The bubble fluxes F_{inj} and F_{ex} scale with whitecap coverage (0 for $u_{10} < 2.27$).

The entrainment term is governed by the change in mixed layer depth (only deepening of the mixed layer impacts the surface water budget) and by difference between mixed layer concentration c_x and the concentration in the subsurface layer $c_{x,sub}$:

$$F_{entr} = \left(c_{x,sub} - c_x \right) d(mld)/dt \tag{10}$$

The changes in mixed layer depth used to quantify the physical entrainment term were obtained from temperature and salinity profiles of the Mercator global operational system PSY3V3. These model-derived mixed layer depths, which assimilate all available measurements in a given study region, showed reasonable agreement with values obtained from our actual CTD observations ($r = 0.61$) and were able to reproduce the spatial patterns in mixing depths across our cruise track (Figure S1 in the supporting information). Moreover, comparison of the time-dependent model MLD history, with observations derived from Argo float data showed that the model output was able to reproduce the significant changes in MLD (including a number of pronounced deepening events) observed across our study region (Figure S2).

For N_2, the choice of the submixed layer concentration $c_{N_2,sub}$ has a minor influence on the calculation given the weak vertical gradients of this gas in the absence of a subsurface biological production or consumption term. We thus chose a uniform value of 100% surface saturation for $c_{N_2,sub}$. In the case of O_2, however, strong vertical gradients and variable saturation levels have a significant influence on the entrainment term, and the choice of $c_{O_2,sub}$ values can thus exert a significant influence on the model calculations under conditions of mixed layer deepening. Given our interest in comparing physical and biological processes affecting the surface water O_2 balance, we computed two different O_2 entrainment terms. The first term, ΔO_{2pe}, reflects the entrainment of subsurface waters in the absence of a biological signature. For this calculations the subsurface O_2 end-member ($c_{O_2,sub}$) was set to 100%, as in the N_2 calculations. We also computed a total

O_2 entrainment term, ΔO_{2te}, which reflects the bulk transport of O_2 into the mixed layer, based on the observed difference in O_2 concentrations between surface and subsurface waters. For these calculations, we used the average O_2 concentration 20–25 m below the mixed layer depth to define the end-member concentration ($c_{O_2,sub}$) for entrained waters. This depth was chosen based on examination of mixed layer depth history from the PSY3V3 output during a number of modeled entrainment events. The mean $c_{O_2,sub}$ end-member values were calculated from CTD data for each sampling station and interpolated to the full resolution of our cruise track for use in the entrainment calculations.

The model mixed layer concentrations of O_2 and N_2 were initialized at 100% saturation starting 30 days prior to the underway measurements. The ancillary data (e.g., wind speed, atmospheric pressure, and mixed layer depth) were interpolated to the cruise track position and time and used to force the model calculations for 30 days with time steps of 6 h.

2.7. Net Community Production Estimates

We used the approach of *Reuer et al.* [2007] to estimate net community production (NCP, i.e., gross photosynthesis minus community respiration) from our mixed layer $\Delta O_2/Ar$ measurements. The calculations presented by *Reuer et al.* [2007] are based on a steady state model, where lateral advection and vertical entrainment are assumed to be negligible, and the mixed layer O_2 mass balance is influenced solely by NCP and gas exchange. Under these conditions, steady state NCP is equivalent to the air-sea flux of biogenic O_2 (obtained from $\Delta O_2/Ar$ and the air equilibrium O_2 concentration, $\alpha_{O_2} \times p_{atm}$). The gas exchange term, k, is derived using a weighting function to account for variability in wind speed history over the residence time of O_2 in the mixed layer (see *Reuer et al.* [2007] for details).

$$NCP = \Delta O_2/Ar \times \alpha_{O_2} \times p_{atm} \times k \tag{11}$$

For consistency with our box model calculations, we used the gas exchange parameterization (k) of *Sweeney et al.* [2007], and the ice-dependent scaling factor of *Loose et al.* [2009] to derived NCP estimates.

We recognize that the assumptions required for the $\Delta O_2/Ar$-based NCP calculations are unrealistic for at least some portions of our cruise track where entrainment of subsurface waters into the mixed layer is likely nonnegligible. To examine the influence of mixed layer entrainment on NCP, we used the output from our box model calculations (see above) to estimate the O_2 flux associated with changes in mixed layer depth. Based on our calculation of ΔO_{2pe} and ΔO_{2te}, we derived a specific biological entrainment term, ΔO_{2be}, for use in the correction of $\Delta O_2/Ar$ for NCP calculations.

$$\Delta O_{2be} = \Delta O_{2te} - \Delta O_{2pe} \tag{12}$$

This term reflects the entrainment of biologically modified O_2 signatures from subsurface waters. The purely physical entrainment term, ΔO_{2pe}, affects O_2 and Ar in a nearly identical manner and thus has a negligible influence on the measured $\Delta O_2/Ar$ ratio. In contrast, ΔO_{2be} specifically affects O_2 and thus modifies $\Delta O_2/Ar$. Our approach, based on the separation of biogenic and nonbiogenic entrainment fluxes, thus allows us to correct the observed $\Delta O_2/Ar$ values for entrainment of biologically modified subsurface waters, after removing the nonbiological entrainment signature. We used the corrected $\Delta O_2/Ar$ data as input to equation (11). Given the physical complexity of our study region, and its high degree of temporal variability, we treat our NCP calculations as a first-order estimate of biological O_2 production rates in the mixed layer, recognizing the quantitative limitations of this approach.

Additional NCP estimates were derived from an analysis of seasonal mixed layer DIC deficits as described in section 2.5. In order to estimate a mean daily NCP rate from these seasonal deficits, it is necessary to choose an integration time scale (i.e., the length of time over which the DIC deficit has accrued). We obtained an estimate of the integration time scale using an analysis of 8 day AquaModis Chl *a* imagery provided by Oregon State University, with a cloud-filling algorithm (http://www.science.oregonstate.edu/ocean.productivity/). We computed mean Chl *a* concentrations in three geographic regions centered around the N-S, E-W, and WAP sections of our cruise track and used these values to reconstruct the history of surface Chl *a* concentrations in each subregion (Figure S3). The approximate initiation date of positive NCP was then derived as the first significant increase in Chl *a* concentrations over wintertime values, and the NCP
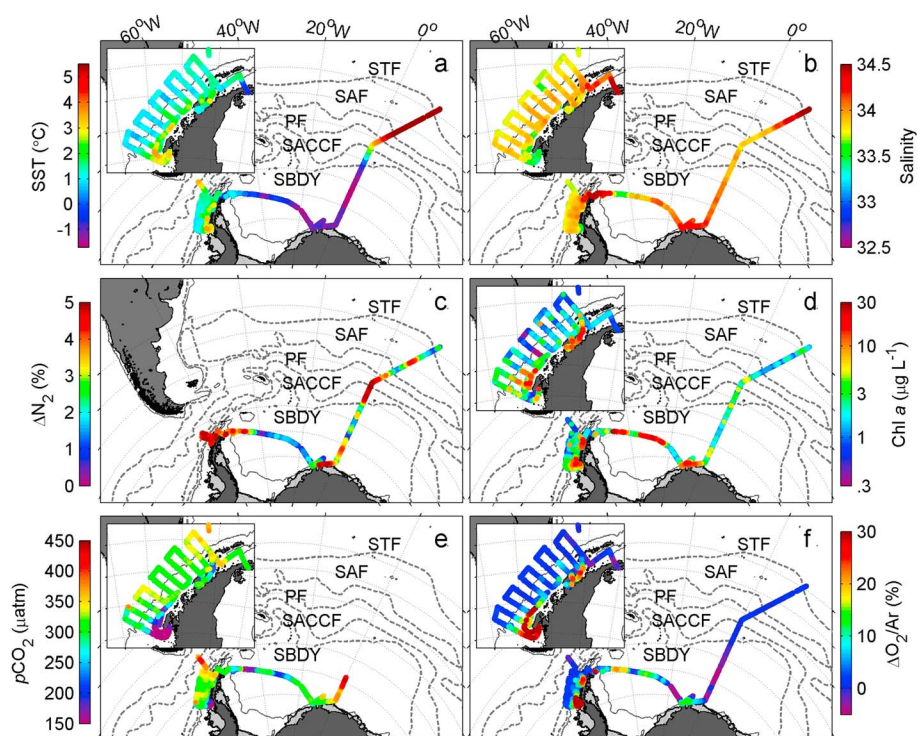
Figure 2. Spatial distribution of (a) sea surface temperature, SST, (b) salinity, (c) N_2 saturation, ΔN_2, (d) Chl a fluorescence, (e) $p CO_2$, and (f) biological O_2 saturation, $\Delta O_2/Ar$ along the cruise track. Inset figures show a detailed view of the property distributions along the WAP transect. Note that $p CO_2$ and ΔN_2 data are not available for the full cruise track due to instrument problems.

integration times for DIC deficits were obtained from the difference between the mean sampling date and the calculated bloom initiation date in each of the three regions. We obtained integration times of 69, 50, and 98 days for the N-S, E-W, and WAP regions, respectively. We used a photosynthetic quotient of 1.4 mol O_2:mol DIC [*Laws*, 1991] to convert DIC-based NCP to O_2 units for comparison with our $\Delta O_2/Ar$-based NCP estimates.

3. Results and Discussion

3.1. Surface Water Hydrography and Chl *a*

Sea surface temperature (SST) exhibited a strong latitudinal gradient along the northern portion of the N-S transect, across the transition from subtropical to Antarctic waters (Figures 2a and 3d). In contrast, the ice-covered waters south of the SBdy frontal zone were characterized by near homogeneous SST (±0.3°C) close to the freezing point of seawater. Along the E-W and WAP transects, SST ranged from −1.8 to 3°C and exhibited significant spatial heterogeneity (Figures 2a and 3d). The relatively warm SST of the WAP region reflects the influence of surface warming in shallow near-shore waters, and/or the signature of modified circumpolar deep water flowing onto the continental shelf [*Martinson and McKee*, 2012]. Salinity also showed significant spatial variability across the E-W and WAP regions. Relatively fresh waters (salinity ~ 33.2), indicative of local sea ice melt, were observed along the Weddell Sea MIZ at ~ 42°W and along the WAP in the near-shore waters adjacent to Marguerite Bay (Figure 2b). Mixed layer depths, computed from CTD profile data, ranged from < 10 m to ~ 100 m, with an overall mean of 26 m (±20 m standard deviation.). The shallowest mixed layer depths were observed in low-salinity regions along the western portion of the Weddell Sea MIZ and in near-shore waters of the WAP.

Strong gradients in surface hydrography were associated with significant variability in phytoplankton Chl *a* fluorescence. Pelagic waters of the N-S transect were generally characterized by relatively low Chl *a* fluorescence, although elevated values were observed along frontal zones of the SAF, PF, SACCF, and SBdy (Figures 2d and 3c). Increased Chl *a* concentrations along frontal zones are a well-known feature of the
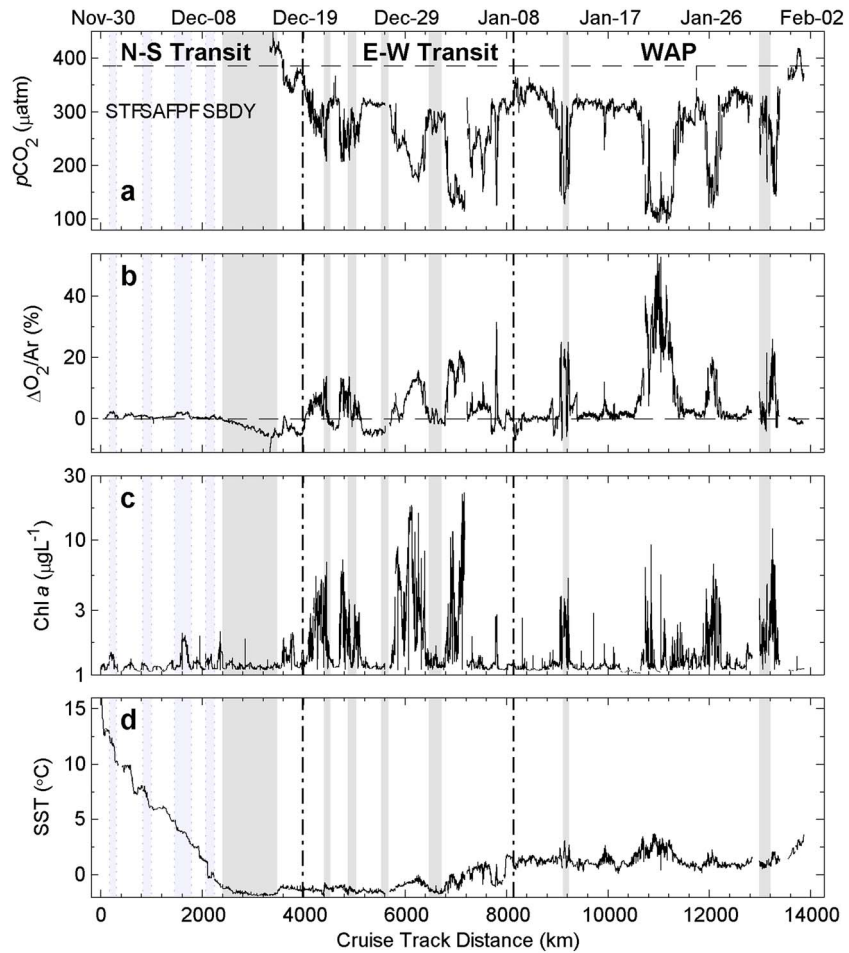
Figure 3. Distribution of (a) pCO_2, (b) biological O_2 saturation, $\Delta O_2/Ar$, (c) Chl a fluorescence, and (d) sea surface temperature along the cruise track. Black vertical lines show the demarcation between the different portions of the cruise track, vertical grey shaded bars show regions with more than 50% ice cover, and blue shaded areas with dotted lines show the position of different frontal regions.

Southern Ocean that has been attributed to the supply of nutrients through enhanced vertical mixing [*Laubscher et al.*, 1993; *Sokolov and Rintoul*, 2007; *Sokolov*, 2008]. The intensity of this mixing is particularly strong in the polar frontal region, where we observed the greatest enhancement of surface Chl a fluorescence. Relative to the N-S transect, waters of the Weddell Sea MIZ and near-shore regions of the WAP showed extreme variability in Chl a fluorescence. Values ranged by more than 2 orders of magnitude and exhibited sharp gradients over small spatial scales, often in regions of local sea ice melt (Figure 3c). Previous studies have demonstrated a strong influence of sea ice processes on phytoplankton growth in surface waters [*Arrigo and van Dijken*, 2004; *Smith and Nelson*, 1985]. Melting ice can stimulate phytoplankton growth through the release of Fe [*Gerringa et al.*, 2012; *Sedwick and DiTullio*, 1997] and/or decreasing surface salinity, which acts to stabilize the mixed layer. Indeed, we observed a negative relationship between Chl a fluorescence and salinity in the WAP ($r = -0.42$) and, to a lesser extent, along the E-W transit ($r = -0.17$). The relationship between biological productivity and mixed layer depth is addressed in section 3.6.

3.2. $\Delta O_2/Ar$ and pCO_2 Distributions

Along the N-S transect, $\Delta O_2/Ar$ was generally within a few percent of atmospheric equilibrium, with slightly positive values north of 55°S (<2000 km along the cruise track) and negative values in ice-covered waters of the Weddell Sea MIZ (Figures 2f and 3b). Negative $\Delta O_2/Ar$ values are indicative of net heterotrophic conditions
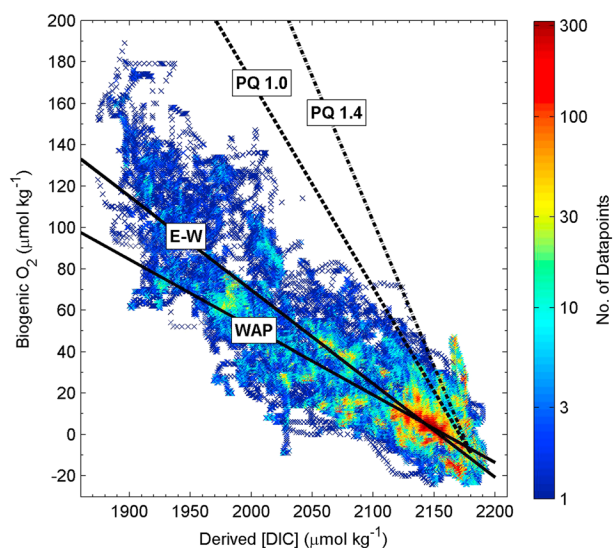
Figure 4. Relationship between dissolved inorganic carbon (DIC) concentrations and biogenic O_2. DIC values were obtained from MIMS pCO_2 data, using empirically derived alkalinity values (based on surface salinity). Biogenic O_2 (i.e., the amount of excess O_2 in the mixed layer derived from biological production) was computed from $\Delta O_2/Ar$ data using a temperature- and salinity-dependent O_2 solubility function. Solid lines show the DIC-O_2 relationship for the E-W and WAP portions of the ship track derived from a Type II regression analysis, while dashed lines show the expected DIC-O_2 relationship for a photosynthetic quotient (PQ) of 1 or 1.4 mol O_2 produced per mol DIC consumed. The slope of the O_2-DIC relationship is 0.45 and 0.33 for the E-W and WAP regions, respectively.

under the sea ice and/or the presence of deep mixed layers bearing a remnant heterotrophic signature. Although relatively few pCO_2 data are available for the N-S transect, we observed a sharp pCO_2 gradient (from 450 to 330 μatm) on the southern edge of the MIZ (Figures 2e and 3a). Surface water pCO_2 and $\Delta O_2/Ar$ showed high variability in the Weddell Sea MIZ (E-W transect) and WAP region. In these areas, pCO_2 reached minimum values of ~100 μatm, while $\Delta O_2/Ar$ in excess of 50% was observed (Figures 3a and 3b). The lowest pCO_2 and highest $\Delta O_2/Ar$ occurred in near-shore waters of Marguerite Bay (WAP; Figures 2e and 2f) at ~11,000 km along our cruise track.

The pCO_2 and $\Delta O_2/Ar$ disequilibria we observed are substantially higher than values previously reported for the offshore pelagic Southern Ocean [*Cassar et al.*, 2011; *Reuer et al.*, 2007; *Shadwick et al.*, 2014], but they are consistent with recent observations from the highly productive waters of the Ross Sea and Amundsen Sea polynyas [*Smith and Gordon*, 1997; *Tortell et al.*, 2011, 2012]. In sections 3.5 and 3.6, we discuss the relative contributions of physical and biological processes to O_2 supersaturation. Here we note only that $\Delta O_2/Ar$ was positively correlated with Chl a ($r = 0.66$ and 0.43 along the E-W and WAP transects, respectively) and showed enhancements in frontal zones along the N-S transect. Unlike $\Delta O_2/Ar$, pCO_2 is sensitive to temperature-dependent solubility changes. During the 30 days prior to our sampling, the NOAA OISST data show an average surface water warming of ~1°C along our cruise track. This warming would lead to a 4% (~15 μatm) increase in pCO_2 [*Takahashi et al.*, 2002], which is small compared to the observed pCO_2 variability along the cruise track. This result indicates that biological uptake exhibited a first-order control on pCO_2 distributions.

As expected, pCO_2 exhibited a strong negative correlation with $\Delta O_2/Ar$ along our cruise track (Pearson's correlation coefficient, $r = -0.85$ and -0.91 for the E-W and WAP regions, respectively). Figure 4 shows the corresponding relationship between O_2 and total dissolved inorganic carbon (DIC) concentrations derived from pCO_2 and $\Delta O_2/Ar$ data. For both the WAP and E-W regions, the slope of the O_2:DIC relationship was significantly lower than the expected photosynthetic stoichiometry (photosynthetic quotient, PQ, 1.0–1.4 mol O_2:mol DIC [*Laws*, 1991]). This discrepancy can be explained by the differential rate of sea-air O_2 and CO_2 exchange. Faster air-sea equilibration of O_2 results in a shorter residence time of this gas in the mixed layer, and a more rapid ventilation of photosynthetically derived O_2. During our cruise, the average residence time of O_2 in the mixed layer was < 1 week, given the mean wind speed (9.2 m s^{-1}) and MLD (26 m) observed across the survey region. In contrast, disequilibria in pCO_2, which is buffered by the seawater carbonate system, can persist for many weeks and even months in the surface mixed layer [*Takahashi et al.*, 2009]. The degree of uncoupling between CO_2 and O_2 in the mixed layer should thus provide insight into temporal evolution of biological productivity in surface waters. Regions where the biological production signal is "older" should exhibit a higher degree of CO_2-O_2 uncoupling. In our data set, the lower O_2-DIC slope in the WAP region (0.33 versus 0.45 for the E-W transect; Figure 4) suggests that the production signal was integrated over a longer time interval. Indeed, remote sensing data show the presence of phytoplankton blooms in the WAP for over 2 months prior to our sampling (see Figure 8b and
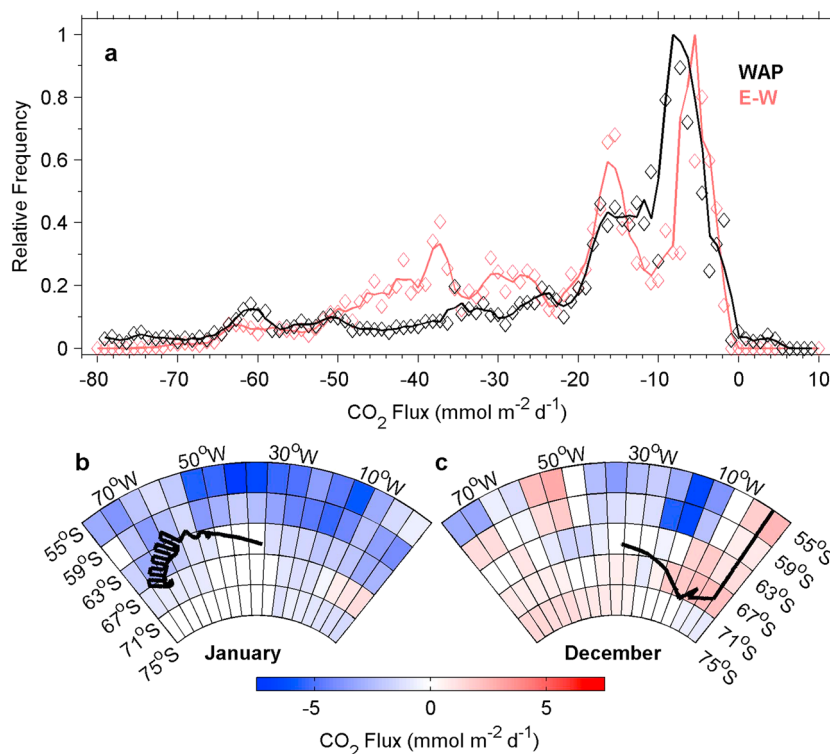
Figure 5. (a) Frequency distribution of air-sea CO_2 fluxes along the E-W and WAP regions of the cruise track. (b and c) The ship track plotted over the monthly climatological CO_2 flux derived from the global climatology of *Takahashi et al.* [2009]. Negative fluxes imply oceanic uptake of CO_2.

section 3.6). In contrast, much of the biological production along the E-W region occurred following recent ice retreat, with shorter time interval for gas exchange to uncouple O_2 and DIC. Similar observations on the time-dependent coupling of CO_2 and O_2 coupling have been recently reported by *Shadwick et al.* [2014] although these authors did not present derived O_2 and DIC concentrations.

3.3. Sea-Air CO_2 Fluxes

During the time of the survey, our sampling region served as a strong CO_2 sink. Along the E-W transit, CO_2 fluxes showed a bimodal distribution (Figure 5), with an overall mean of -13.0 ± 6.70 (standard deviation) $mmol\,m^{-2}\,d^{-1}$, and a range of -41.4 to $-2.76\,mmol\,m^{-2}\,d^{-1}$ (negative fluxes signify oceanic uptake). For the WAP region, the mean CO_2 flux was $-9.26 \pm 5.51\,mmol\,m^{-2}\,d^{-1}$ (range -32.3 to $+7.43$). In both the WAP and E-W regions, the frequency distribution of CO_2 fluxes (Figure 5) exhibited a long tail at low values (oceanic uptake). The strongest oceanic CO_2 uptake along the entire cruise track ($>40\,mmol\,m^{-2}\,d^{-1}$) was observed near Marguerite Bay along the WAP, while a small net CO_2 efflux from surface waters was observed north of the WAP in pelagic waters of the Drake Passage.

Current estimates of regional air-sea CO_2 fluxes in the Southern Ocean are based on the climatology of *Takahashi et al.* [2009], compiled from a global compilation of field measurements. This climatology indicates a weak to moderate Southern Ocean CO_2 sink between ~ 40 and 50°S (between the STF and PF) and suggests that waters south of the PF are either neutral or slight sources of CO_2 to the atmosphere. However, actual data coverage is sparse over much of the high-latitude Southern Ocean, particularly in the MIZ and the continental shelf regions. Examination of the underlying pCO_2 data set used to construct the 2009 climatology shows very few summer time (December and January) pCO_2 observations in the Weddell Sea MIZ, with many grid cells lacking primary data, and fluxes derived from interpolation of the nearest available observations. Moreover, the resolution of the climatology grid cells ($4° \times 5°$) is coarse relative to the observed length scales of variability. For these reasons, it is likely that significant features are not well represented in the climatological maps of Southern Ocean CO_2 fluxes.

Table 1. Comparison of Sea-Air CO_2 Fluxes ± Standard Deviation From the MIMS Data (E-W and WAP Transects) and the Monthly Climatology of *Takahashi et al.* [2009][a]

	MIMS Data		Climatology	
	CO_2 Flux (mmol m^{-2} d^{-1})	ΔpCO_2 (µatm)	CO_2 Flux (mmol m^{-2} d^{-1})	ΔpCO_2 (µatm)
December	-10.0 ± 5.8	-91 ± 59	1.4 ± 0.9	17 ± 11
January	-9.9 ± 4.2	-108 ± 24	-2.4 ± 0.9	-39 ± 14

[a]Average fluxes from MIMS data were derived from values binned into $4° \times 5°$ boxes to match the resolution of the climatology. Averages reported for the climatology were obtained from grid cells containing MIMS data.

In Figure 5, we have plotted our cruise track over the gridded CO_2 fluxes of *Takahashi et al.* [2009]. Our sampling region encompassed ~25 grid cells (seven of which lacked primary data), and we derived mean CO_2 fluxes and air-sea CO_2 gradients (ΔCO_2) for these areas. The results, shown in Table 1, highlight a significant difference between the CO_2 fluxes derived from our MIMS data, and those from the climatology. In December, the climatology shows our sampling region to be near neutral with respect to air-sea CO_2 fluxes (1.4 ± 0.90 mmol m^{-2} d^{-1}), whereas our measurements show mean oceanic uptake of $10 (\pm 5.8)$ mmol m^{-2} d^{-1}. In January, the climatological CO_2 flux is -2.4 ± 0.92 mmol m^{-2} d^{-1}, compared to -9.9 ± 4.2 mmol m^{-2} d^{-1} derived from our measurements. The climatology represents a mean value derived from many years of observations, and some interannual variability is expected. During our survey, we measured significantly higher air-sea CO_2 disequilibria than are present in the climatology; for December and January, respectively, we observed an average ΔCO_2 of -91 and -108 µatm, compared to the climatological values of ~+17 and -39 µatm. These differences are likely too large to represent simple interannual variability and likely reflect real differences in the underlying distribution of data. Our results thus suggest significantly higher oceanic CO_2 uptake in high-latitude Antarctic waters than is represented by the global climatology. Similar observations have been reported in previous studies [*Arrigo et al.*, 2008; *Bellerby et al.*, 2004; *Hoppema et al.*, 2000a]. Note that the apparent difference in sea-air CO_2 fluxes between our observations and the climatology is approximately twofold larger if we compute the fluxes using ship-based winds as opposed to the weekly averaged NCEP reanalysis product.

High-latitude Antarctic waters, and the MIZ in particular, should be effective at sequestering CO_2 from the atmosphere due to the coupling of biological productivity with sea ice dynamics. As observed in our study and that of previous authors [*Bakker et al.*, 2008; *Jones et al.*, 2010], ice retreat leads to enhanced phytoplankton biomass and strong CO_2 uptake. Previous studies have shown that much of the CO_2 taken up by spring phytoplankton growth can effectively be sequestered into subsurface layers during late summer cooling and the return of ice cover at the end of the growing season [*Sweeney*, 2003]. Late season sea ice cover acts to limit outgassing of high CO_2 during the net heterotrophic period of the annual growing season, enhancing the CO_2 sequestration efficiency of surface waters. For this reason, Antarctic continental shelf waters are likely to contribute disproportionately to Southern Ocean CO_2 uptake [*Arrigo et al.*, 2008]. Inclusion of more data from these regions into updated climatologies (with finer-scale grid cell resolution, and greater seasonal data coverage) could lead to revised estimates of Southern Ocean CO_2 uptake, with significant implications for the global C budget.

3.4. ΔN_2 Distribution

Across much of our sampling region, N_2 was supersaturated with respect to atmospheric equilibrium (i.e., $\Delta N_2 > 0$; Figures 2c and 6a). The one exception occurred in an ice-covered region of the Weddell Sea (~6500 km), where we measured a ΔN_2 of ~-1%. This feature may reflect the low atmospheric pressure ~7 days prior to our arrival on station, or the recent release of cold and fresh meltwater that is undersaturated in N_2 (due to gas exclusion from the forming ice matrix). The average ΔN_2 along the full cruise track was ~+2.5%, with maximum values of ~+6% observed in regions of high wind speed (>20 m s^{-1}) and/or decreasing atmospheric pressure along the northern portion of the N-S transect (in the SACCF region), the Weddell Sea continental margin and the northern WAP (Figure 6). In some cases (e.g., ~11,000 km cruise track distance), strong N_2 supersaturation was associated with recent warming of the mixed layer and decreased gas solubility. The maximum ΔN_2 values we observed are significantly higher than those reported previously for midlatitude oceanic regions [*Emerson et al.*, 2008; *McNeil et al.*, 2005;
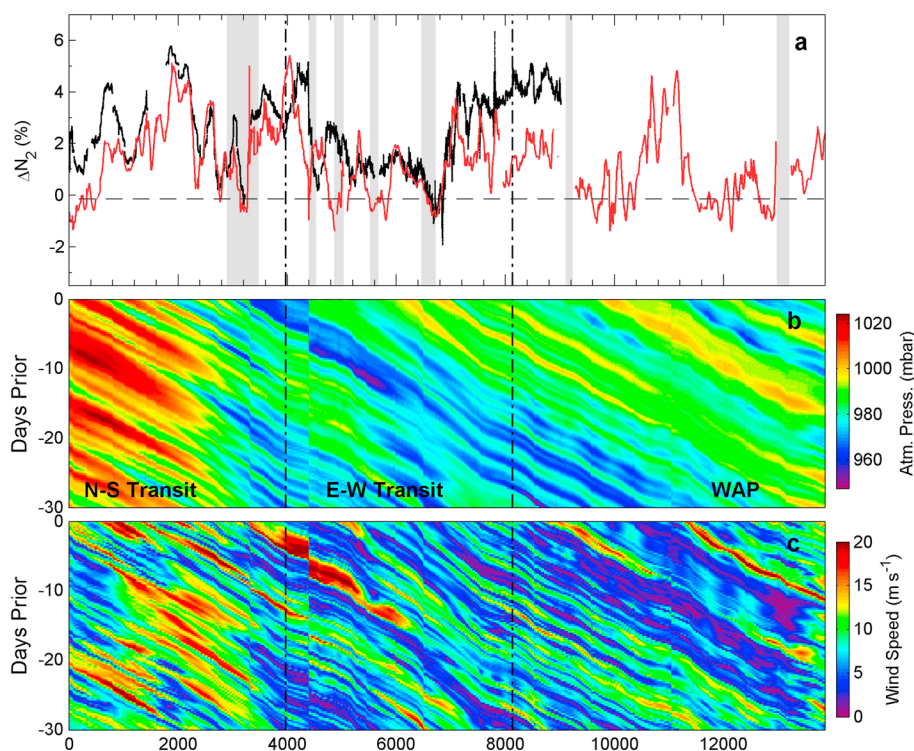
Figure 6. (a) Nitrogen saturation, ΔN_2, (b) atmospheric pressure history, and (c) wind speed history along the cruise track. The black line in Figure 6a shows the ΔN_2 value derived from Gas Tension Device (GTD) measurements, while the red line shows the results of box model calculations (see text for a full description). Grey vertical patches in Figure 6a show regions with greater than 50% ice cover. Atmospheric pressure and wind speed data shown in Figures 6b and 6c were derived from NCEP reanalysis. The y axis in Figures 6b and 6c represents the number of days prior to the ship's arrival at a location along the cruise track.

Vagle et al., 2010], including recent observations from the Sub-Antarctic zone of the Southern Ocean [*Weeding and Trull*, 2014], where ΔN_2 did not exceed ~ +3% during an observation period of 7 months. Our observations may be indicative of a persistently high ΔN_2 signal across large areas of the Southern Ocean, driven by high regional wind speeds and strong changes in atmospheric pressure.

Box model calculations of ΔN_2, based on gas exchange processes and mixed layer entrainment [*Nicholson et al.*, 2011], were used to examine the various processes contributing to the high ΔN_2 across our survey region. In general, the calculated ΔN_2 values were in good agreement with our observations, and the model was able to reproduce both the absolute magnitude of ΔN_2 and its spatial variability along much of our cruise track (Figure 6a). In a number of instances, however, modeled ΔN_2 was significantly lower than the observed values, particularly at the beginning and end of the HGTD data record. While it is possible that offsets between observations and model output at the end of the data reflect problems with the HGTD before its failure, several sources of uncertainty are also present in our calculations. The 1-D model we used for our calculations does not account for advection of water masses with possibly different preformed gas concentrations. The dynamic system of frontal zones between Cape Town and the Polar Front may thus explain part of the discrepancy between observations and model output during the northern portion of the N-S transect. The remainder of our survey region is less prone to advection, owing to a (zonally) more homogeneous water mass structure. In the MIZ, uncertainty in the model calculations may result from sea ice-dependent processes. The sea ice history used in the model was derived from reprocessed satellite data with a relatively coarse spatial resolution. Sea ice cover exerts a significant influence on the strength of air-sea exchange, and errors in the representation of sea ice cover or in the parameterization of ice effects on gas exchange coefficients [*Loose et al.*, 2009] would lead to uncertainty in the ΔN_2 calculation. Notwithstanding these sources of uncertainty, we conclude that our observations provide a reasonable validation of the *Nicholson et al.* [2011] model in various Southern Ocean regions with high wind speeds and strong temporal changes in atmospheric pressure. Additional GTD data and
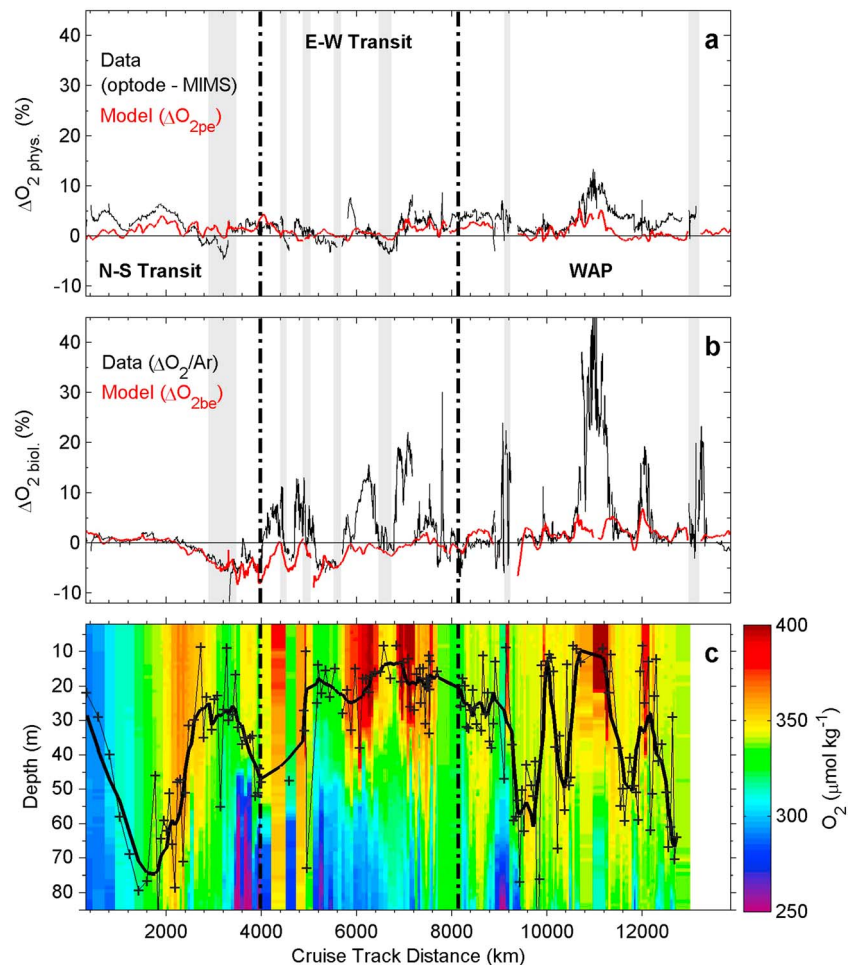
Figure 7. Effects of physical and biological processes on mixed layer O_2 saturation state. (a) The black line shows observed values of ΔO_{2phys}, derived from MIMS $\Delta O_2/Ar$ and optode ΔO_2, while the red line shows the results of box model calculations, including physical terms in the O_2 budget (i.e., air-sea processes and entrainment of nonbiologically modified subsurface waters, ΔO_{2pe}). (b) Biological effects on the surface O_2 budget resulting from in situ NCP (as reflected by surface $\Delta O_2/Ar$ measurements) and modeled entrainment of biologically modified subsurface waters (ΔO_{2be}). (c) O_2 depth profiles along the cruise track derived from CTD observations. The thin black line and crosses represent the computed mixed layer depth, while the thicker line represents a five-point running mean.

higher-resolution physical models will be needed to further examine the distribution of ΔN_2 across various Southern Ocean regions. Inclusion of GTD sensors on new biogeochemical ocean floats and gliders [*Emerson et al.*, 2002; *Nicholson et al.*, 2008] will be particularly useful in this respect.

3.5. Physical Versus Biological Controls on O_2 Saturation States

Unlike N_2, oxygen saturation states are strongly influenced by both physical and biological processes. We quantified the physical effects on O_2 saturation state (ΔO_{2phys}), using simultaneous MIMS and optode measurements (see section 2). Measured values of ΔO_{2phys} (i.e., optode ΔO_2-MIMS $\Delta O_2/Ar$) showed significant variability along our cruise track (Figure 7a), with values ranging from $\sim -5\%$ (undersaturation) to $> +10\%$ (supersaturation). This range of values is significantly larger than that reported recently by *Shadwick et al.* [2014], who measured $\pm 3\%$ ΔO_{2phys} along a transect from Australia to the Antarctic MIZ. In our study, maximum O_2 supersaturation was observed in the WAP region (~11,000 km cruise track), whereas undersaturation was largely confined to several regions of local sea ice cover (Figure 7a). Box model calculations of ΔO_{2pe} (i.e., the entrainment of nonbiologically modified subsurface waters) showed reasonably good agreement with observations and were able to reproduce the spatial pattern of ΔO_{2phys} along much of the cruise track (Figure 7a). There were, however, notable offsets between the modeled

and observed values in some areas, with the model tending to underpredict the observations, as seen for ΔN_2 (Figure 6). The largest discrepancies between the model and observations occurred along the N-S transect, and in the WAP region. As discussed above for ΔN_2, the discrepancy between modeled and observed ΔO_2 along the N-S transect may have resulted from the lateral advection of heterogeneous water masses. By comparison, the high apparent values of ΔO_{2phys} measured in the WAP (in excess of +10%) are more difficult to reconcile with known physical processes driving O_2 supersaturation in the mixed layer. Given the extremely high O_2 concentrations in this region (>60% O_2 supersaturation), the optode was measuring at the outer limit of its calibration range, and we cannot exclude measurement errors leading to an overestimation of ΔO_{2phys}. Moreover, the shallow mixed layers and bottom depths in the coastal WAP make this region susceptible to physically induced O_2 supersaturation resulting from bubble injection under high wind speeds. Under these conditions, our calculations, which assume 100% O_2 saturation in subsurface waters, would underestimate ΔO_{2pe}.

In addition to our calculations of ΔO_{2pe}, we used the box model to derive an O_2 entrainment term associated with the transport of biologically modified waters into the mixed layer. This entrainment term, ΔO_{2be}, can be used to correct $\Delta O_2/Ar$-derived NCP estimates, neglecting the contribution of purely physical entrainment processes (ΔO_{2pe}) that have no significant effect on $\Delta O_2/Ar$. The distribution of modeled ΔO_{2be} along the cruise track is shown in Figure 7b, along with our $\Delta O_2/Ar$ observations. For much of our survey region, the magnitude of the biologically modified entrainment flux was small compared to the mixed layer $\Delta O_2/Ar$ signal. There were, however, a number of areas (particularly along the N-S transect), where the two O_2 fluxes were similar in magnitude. The variability in modeled ΔO_{2be} results from differences in O_2 depth profiles and mixed layer depth history along the cruise track. Under conditions where subsurface O_2 is lower than mixed layer values, due to net heterotrophy in the subeuphotic zone, entrainment of biologically modified subsurface waters acts to decrease the O_2 saturation in the mixed layer (i.e., $\Delta O_{2be} < 0$). This phenomenon was clearly observed in the ice-covered waters of the N-S and E-W transects (Figure 7b), where ΔO_{2be} showed a clear negative signature. In contrast, we observed a number of regions, mostly in the WAP, where ΔO_{2be} was positive, reflecting the entrainment of a remnant productivity signal prior to mixed layer shoaling. *Jonsson et al.* [2013] have also noted the importance of entrainment as a potential source of O_2 into the mixed layer. Quantification of this O_2 source depends on an understanding of mixed layer depth history and the choice of an appropriate subsurface O_2 end-member ($c_{O_2,sub}$). Based on an analysis of the mixed layer time series produced by the PSY3V3 model output, we chose a subsurface O_2 end-member ($c_{O_2,sub}$) 20–25 m below the mixed layer. We note, however, that these end-member O_2 values and the corresponding mixed layer histories are subject to potentially significant uncertainty. Nonetheless, as discussed below, we found that the derived ΔO_{2be} term was able to produce entrainment-corrected $\Delta O_2/Ar$-NCP values that showed good agreement with independent estimates based on DIC deficit calculations. It is also important to note that the entrainment term was generally small compared to the biological O_2 production signal (i.e., $\Delta O_2/Ar$) in the mixed layer for much of our survey region.

3.6. Net Community Production

In recent years, a number of studies have examined Southern Ocean NCP using mixed layer $\Delta O_2/Ar$ measurements, both from discrete samples and continuous underway analysis. This work has been largely based on the approach developed by *Kaiser et al.* [2005] and *Reuer et al.* [2007], where the mixed layer O_2 budget is assumed to be in a steady state, with negligible vertical or lateral fluxes. Under these conditions, the biologically induced flux of O_2 to the atmosphere (O_2 bioflux, as defined by equation (11)) provides a measure of NCP. The assumptions used in these calculations are problematic in weakly stratified and highly dynamic waters encountered over large portions of the Southern Ocean. *Jonsson et al.* [2013] have shown that O_2 bioflux provides good regional estimates of Southern Ocean NCP ($\pm \sim 25\%$), but significant offsets can exist at smaller scales due to a temporal decoupling between O_2 production and air-sea exchange and to vertical O_2 fluxes across the base of the mixed layer. Using our box model results (section 3.5), we were able to estimate the contribution of entrainment fluxes to the surface biological O_2 budget, and we used this information to correct NCP estimates derived from surface $\Delta O_2/Ar$ data. However, our calculations do not include other physical processes such as upwelling and diapycnal mixing that can also influence NCP derived from $\Delta O_2/Ar$ measurements [*Jonsson et al.*, 2013].
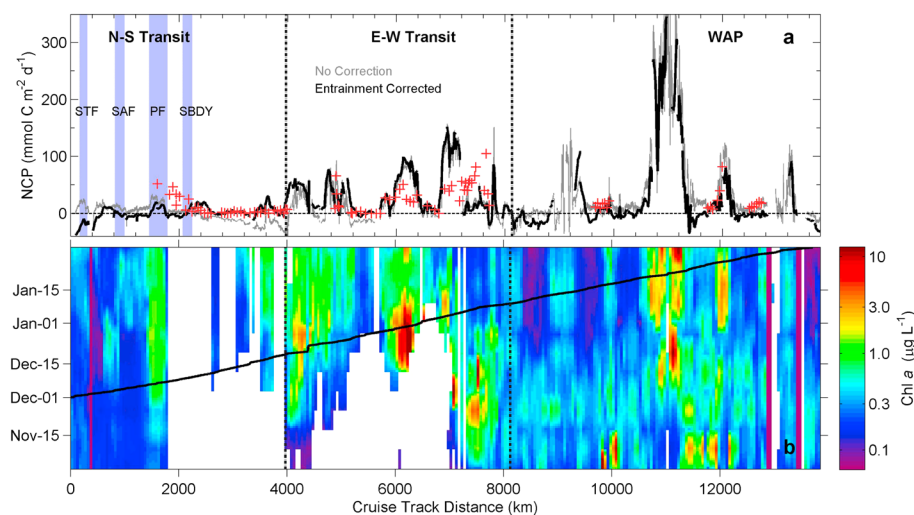
Figure 8. (a) Distribution of net community production (NCP) along the cruise track and (b) the time history of Chl *a* concentrations derived from the AquaModis remote sensing product. Black and grey lines in Figure 8a represent NCP estimates derived from $\Delta O_2/Ar$ data, with and without a correction for biologically modified O_2 entrainment fluxes (ΔO_{2be}). The red crosses in Figure 8a represent NCP estimated from seasonal DIC deficits in the mixed layer. Vertical blue patches in Figure 8a show frontal regions. The black line in Figure 8b shows the location of the research vessel, while white patches denote sea ice cover. Note the logarithmic scaling of the Chl *a* axis.

Figure 8 presents NCP estimates along our cruise track derived from $\Delta O_2/Ar$, with and without a correction for biologically modified entrainment fluxes (ΔO_{2be}). The figure also shows satellite-derived Chl *a* observations, which provide information on the temporal evolution of phytoplankton biomass prior to our sampling. Across the full survey region, O_2/Ar-derived NCP ranged from ~ -40 to > 300 mmol O_2 m^{-2} d^{-1}. The lowest NCP values were found along the N-S transect (maximum ~ 20 mmol O_2 m^{-2} d^{-1}). Despite the low overall productivity observed along much of this transect, there were localized regions of elevated NCP associated with regional frontal features—most notably in the vicinity of the Polar Front zone where vertical mixing can supply Fe to iron-limited surface waters [*Debaar et al.*, 1995]. Without a correction for entrainment, waters of the Weddell Sea MIZ (both along the N-S and E-W transects) appeared to be net heterotrophic (i.e., NCP < 0). However, this apparent net heterotrophic signature was eliminated after accounting for the entrainment fluxes (ΔO_{2be}). In contrast, the entrainment-corrected NCP remained below zero in the STF zone, and in several other localized regions along the cruise track. Net heterotrophy in the STF zone seems unlikely, given the enhanced Chl *a* concentrations in this region (Figure 3c). Rather, we suggest that an overestimation of the O_2 entrainment term (ΔO_{2be}), resulting from errors in the selection of a sub-MLD end-member or in the derived mixed layer depth history, is a more likely explanation for this feature. Regions of net heterotrophy observed along other portions of our cruise track (e.g., between 8000 and 9000 km) were largely confined to waters with very low (<0.3 μg L^{-1}) Chl *a* concentrations. In contrast, the most productive waters, with NCP in excess of 300 mmol O_2 m^{-2} d^{-1} were observed in the central WAP region, where high phytoplankton biomass was detected for over 2 months prior to our sampling. In these high NCP waters, the entrainment correction term was generally small compared to the biological production term.

The variability of our $\Delta O_2/Ar$-derived NCP values is somewhat higher than previous observations for the Southern Ocean, but the mean values for each of survey regions are within the range of recently published estimates. Excluding the negative NCP values in the STF zone, the average NCP for the N-S, E-W, and WAP transects was 9.3, 31, and 14 mmol O_2 m^{-2} d^{-1}, respectively. The low mean NCP value for the WAP region seems initially surprising, given the extremely elevated NCP observed at $\sim 11,000$ km along the cruise track. Outside of this one productivity hot spot, however, much of the WAP region had relatively low (and in some cases even negative) NCP. Excluding the negative values, the mean NCP value in the WAP is 48 mmol O_2 m^{-2} d^{-1}. By comparison, exclusion of negative NCP values from the E-W transect only increased
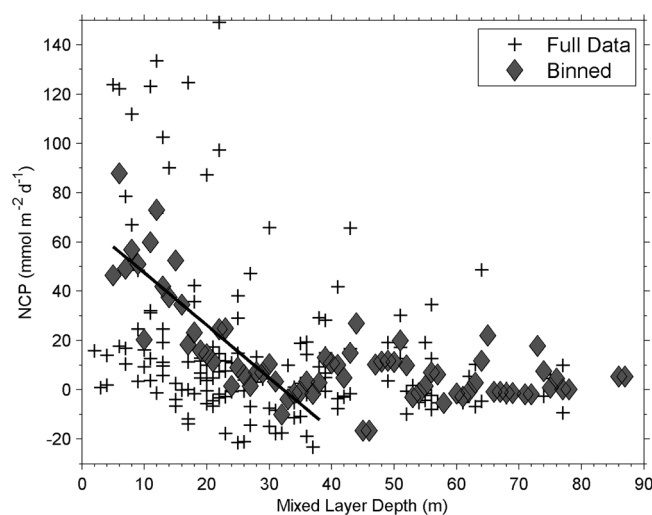
Figure 9. Relationship between $\Delta O_2/Ar$-derived NCP (corrected for biological entrainment fluxes) and mixed layer depth along the cruise track. Full data represent all of the individual NCP estimates derived at CTD stations, while binned data represent average NCP values for each 1 m MLD bin (MLD > 5 m). The solid line represents the best fit regression between binned NCP and MLD ($r = -0.86$).

the mean NCP by ∼ 10%. These results suggest that localized net heterotrophy was more significant to regional NCP budgets in the WAP region.

Based on discrete sampling of surface $\Delta O_2/Ar$, *Reuer et al.* [2007] reported mean NCP estimates ranging from 20 to 36 mmol O_2 m^{-2} d^{-1} for the Sub-Antarctic Zone, Polar Frontal Zone, and Antarctic Zone. More recently, *Shadwick et al.* [2014] have reported a range of NCP estimates from 15 to 75 mmol O_2 m^{-2} d^{-1} (assuming a photosynthetic quotient of 1.4) along a transect from Australia to the Antarctic continent, while *Cassar et al.* [2011] report NCP of approximately up to 150 mmol O_2 m^{-2} d^{-1} for sub-Antarctic waters south of Australia. The maximum NCP values measured along our cruise track (>300 mmol O_2 m^{-2} d^{-1}) are among the highest reported for the Southern Ocean, yet these values are not without precedent. Recent time series work at the Palmer Station LTER site along the WAP [*Tortell et al.*, 2014] show maximum NCP values similar to the highest values we observed along the WAP region of our cruise track.

Independent NCP estimates, based on calculated seasonal DIC deficits at discrete sampling stations, showed good general coherence with our $\Delta O_2/Ar$-derived values. Both the spatial distribution and range of NCP values were similar for the two methods. The agreement between the two estimates was particularly good in the WAP region (unfortunately, DIC samples were not collected in the vicinity of Marguerite Bay, where the highest NCP values were observed), and also south of the SBdy frontal zone along the N-S transect. In contrast, there were apparent offsets between the two NCP estimates in the vicinity of the PF and in the highest productivity regions of the E-W transit. In addition to the uncertainties discussed above for $\Delta O_2/Ar$-derived NCP, NCP estimates from DIC deficits are also subject to potential errors. The most significant source of uncertainty in these calculations relates to the time period over which DIC uptake is normalized. In our analysis, we assumed that DIC deficits began to accumulate following the initiation of the spring phytoplankton blooms (as judged by satellite-based chlorophyll measurements; Figure S3). This approach does not account for potential productivity under sea ice [*Arrigo et al.*, 2012], which is not visible by remote sensing. Although our approach is, by necessity, somewhat simplistic, we are encouraged by the good correspondence of DIC and $\Delta O_2/Ar$-derived estimates of surface water productivity. Our results suggest that mixed layer $\Delta O_2/Ar$ measurements have the capacity to provide meaningful NCP estimates with high spatial resolution.

Beyond the absolute value of our derived NCP estimates, the spatial distribution of biological productivity across our survey region is of interest. Since macronutrients were plentiful across our entire survey region (minimum $NO_3^- > 8\,\mu M$), light and/or iron availability are the most likely bottom-up controls on phytoplankton productivity. Although no iron data are available for our cruise, we assume, based on previous studies, that Fe availability was highest in regions of sea ice melt along the continental shelf [*Gerringa et al.*, 2012; *Klunder et al.*, 2011], where high NCP was observed. To examine the influence of light availability on surface water productivity, we derived NCP estimates for the regions surrounding each of our hydrographic stations (within 5 km) and correlated these values to the mixed layer depths obtained from CTD data. As shown in Figure 9, we observed a weak negative trend between NCP and MLD, particularly for stations with mixed layer depths less than 40 m. Taking only stations with MLD < 40 m, the correlation between MLD and NCP was statistically significant (for 1 m binned data, $r = -0.86$, $p < 0.001$). This

relationship provides some evidence for light-dependent productivity, as suggested previously *Cassar et al.* [2011], *Huang et al.* [2012], and *Shadwick et al.* [2014]. We note, however, that instantaneous MLD estimates do not necessarily provide a good indication of light availability over time scales relevant to our NCP calculations. A more refined analysis could be used, taking into account the time-dependent history of MLD, surface irradiance, and water column light extinction (based on Chl *a* concentrations). Even without this added complexity, our derived NCP estimates likely reflect the dominant influence of light, nutrient supply, and sea ice cover on biological productivity across strongly distinct regions of the Southern Ocean.

4. Conclusions and Future Directions

Our results provide new information on the distribution of pCO$_2$, O$_2$, and N$_2$ in contrasting Southern Ocean regions, and insight into the underlying factors driving these distributions. Across our survey region, strong hydrographic variability led to large gradients in phytoplankton biomass, which, in turn, exerted a significant influence on surface water pCO$_2$ and ΔO$_2$/Ar distributions. This biological signature was modified by physical processes including sea-air exchange and mixed layer entrainment. Using our observations and box model calculations, we were able to quantify the physical contributions to surface water O$_2$ and N$_2$ disequilibria, and we used this information to refine our estimates of NCP from surface ΔO$_2$/Ar observations. The NCP rates derived in this manner were consistent with independent measurements based on surface DIC deficits, providing a high spatial resolution description of biological productivity across the cruise track. Our surface water pCO$_2$ observations suggest that the high-latitude Southern Ocean may be a stronger sink for atmospheric CO$_2$ than is currently represented in the global climatology [*Takahashi et al.*, 2009]. To the extent that our results are applicable on a broad regional scale, there may thus be a need to critically reevaluate current estimates of Southern Ocean CO$_2$ uptake.

The increasing availability of autonomous shipboard instruments for surface gas measurements (e.g., optodes, GTDs, and seagoing mass spectrometers) has significantly expanded the spatial and temporal coverage of oceanic dissolved gas observations. In the future, continued deployments of these autonomous instruments, along with instrumented floats, gliders, and moorings [*Emerson et al.*, 2008; *Nicholson et al.*, 2008], will allow us to assemble a more robust database of Southern Ocean ΔN$_2$, ΔO$_2$, ΔO$_2$/Ar to help constrain NCP and air-sea exchange processes. Moreover, additional pCO$_2$ measurements in poorly sampled regions will help to refine mean climatological CO$_2$ fluxes for the Southern Ocean. In conjunction with increased data coverage, more sophisticated modeling approaches could be used to interpret surface gas distributions, taking into account smaller-scale physical processes that act to perturb the mixed layer mass balance. Improved data sets and models will facilitate more robust NCP and CO$_2$ flux estimates and increase our understanding of the Southern Ocean's role in global biogeochemical cycles.

References

Arrigo, K. R., and G. L. van Dijken (2003), Phytoplankton dynamics within 37 Antarctic coastal polynya systems, *J. Geophys. Res.*, *108*(C8), 3271, doi:10.1029/2002JC001739.

Arrigo, K. R., and G. L. van Dijken (2004), Annual changes in sea-ice, chlorophyll *a*, and primary production in the Ross Sea, Antarctica, *Deep Sea Res., Part II*, *51*(1–3), 117–138.

Arrigo, K. R., G. van Dijken, and M. Long (2008), Coastal Southern Ocean: A strong anthropogenic CO$_2$ sink, *Geophys. Res. Lett.*, *35*, L21602, doi:10.1029/2008GL035624.

Arrigo, K. R., D. K. Perovich, R. S. Pickart, Z. W. Brown, G. L. van Dijken, K. E. Lowry, M. M. Mills, M. A. Palmer, W. M. Balch, and F. Bahr (2012), Massive phytoplankton blooms under Arctic sea ice, *Science*, *336*(6087), 1408–1408.

Bakker, D. C. E., M. Hoppema, M. Schroder, W. Geibert, and H. J. W. De Baar (2008), A rapid transition from ice covered CO$_2$-rich waters to a biologically mediated CO$_2$ sink in the eastern Weddell Gyre, *Biogeosciences*, *5*(5), 1373–1386.

Bellerby, R. G. J., M. Hoppema, E. Fahrbach, H. J. W. de Baar, and M. H. C. Stoll (2004), Interannual controls on Weddell Sea surface water fCO$_2$ during the autumn-winter transition phase, *Deep Sea Res., Part I*, *51*(6), 793–808.

Boyd, P. W. (2002), Environmental factors controlling phytoplankton processes in the Southern Ocean, *J. Phycol.*, *38*(5), 844–861.

Brewer, P. G., A. L. Bradshaw, and R. T. Williams (1986), Measurements of total carbon dioxide and alkalinity in the North Atlantic Ocean in 1981, in *The Changing Carbon Cycle*, pp. 358–381, Springer, New York.

Caldeira, K., and P. B. Duffy (2000), The role of the Southern Ocean in uptake and storage of anthropogenic carbon dioxide, *Science*, *287*(5453), 620–622.

Carrillo, C. J., R. C. Smith, and D. M. Karl (2004), Processes regulating oxygen and carbon dioxide in surface waters west of the Antarctic Peninsula, *Mar. Chem.*, *84*(3–4), 161–179.

Cassar, N., M. L. Bender, B. A. Barnett, S. Fan, W. J. Moxim, H. Levy, and B. Tilbrook (2007), The Southern Ocean biological response to Aeolian iron deposition, *Science*, *317*(5841), 1067–1070.

Cassar, N., P. J. DiFiore, B. A. Barnett, M. L. Bender, A. R. Bowie, B. Tilbrook, K. Petrou, K. J. Westwood, S. W. Wright, and D. Lefevre (2011), The influence of iron and light on net community production in the Subantarctic and Polar Frontal Zones, *Biogeosciences*, *8*(2), 227–237.

Castro-Morales, K., N. Cassar, D. R. Shoosmith, and J. Kaiser (2013), Biological production in the Bellingshausen Sea from oxygen-to-argon ratios and oxygen triple isotopes, *Biogeosciences*, *10*(4), 2273–2291.

Coale, K. H., R. M. Gordon, and X. J. Wang (2005), The distribution and behavior of dissolved and particulate iron and zinc in the Ross Sea and Antarctic circumpolar current along 170 degrees W, *Deep Sea Res., Part I*, *52*(2), 295–318.

Craig, H., and T. Hayward (1987), Oxygen supersaturation in the ocean: Biological versus physical contributions, *Science*, *235*(4785), 199–202.

Debaar, H. J. W., J. T. M. Dejong, D. C. E. Bakker, B. M. Loscher, C. Veth, U. Bathmann, and V. Smetacek (1995), Importance of iron for phytoplankton blooms and carbon dioxide drawdown in the Southern Ocean, *Nature*, *373*(6513), 412–415.

Dickson, A. G. (1994), Determination of dissolved oxygen in sea water by Winkler titration, *WHP Operations and Methods*, 1–14.

Dickson, A. G., and F. J. Millero (1987), A comparison of the equilibrium constants for the dissociation of carbonic acid in seawater media, *Deep Sea Res., Part A*, *34*(10), 1733–1743.

Dickson, A. G., C. L. Sabine, and J. R. Christian (2007), Guide to best practices for ocean CO_2 measurements.

Emerson, S., C. Stump, B. Johnson, and D. M. Karl (2002), In situ determination of oxygen and nitrogen dynamics in the upper ocean, *Deep Sea Res., Part I*, *49*(5), 941–952.

Emerson, S., C. Stump, and D. Nicholson (2008), Net biological oxygen production in the ocean: Remote in situ measurements of O_2 and N_2 in surface waters, *Global Biogeochem. Cycles*, *22*, GB3023, doi:10.1029/2007GB003095.

Garcia, H. E., and L. I. Gordon (1992), Oxygen solubility in seawater: Better fitting equations, *Limnol. Oceanogr.*, *37*(6), 1307–1312.

Gerringa, L. J. A., A. C. Alderkamp, P. Laan, C. E. Thuroczy, H. J. W. De Baar, M. M. Mills, G. L. van Dijken, H. van Haren, and K. R. Arrigo (2012), Iron from melting glaciers fuels the phytoplankton blooms in Amundsen Sea (Southern Ocean): Iron biogeochemistry, *Deep Sea Res., Part II*, *71-76*, 16–31, doi:10.1016/j.dsr2.2012.03.007.

Hamme, R. C., and S. R. Emerson (2004), The solubility of neon, nitrogen and argon in distilled water and seawater, *Deep Sea Res., Part I*, *51*(11), 1517–1528.

Hamme, R. C., and S. R. Emerson (2006), Constraining bubble dynamics and mixing with dissolved gases: Implications for productivity measurements by oxygen mass balance, *J. Mar. Res.*, *64*(1), 73–95.

Honjo, S., S. J. Manganini, R. A. Krishfield, and R. Francois (2008), Particulate organic carbon fluxes to the ocean interior and factors controlling the biological pump: A synthesis of global sediment trap programs since 1983, *Prog. Oceanogr.*, *76*(3), 217–285.

Hoppema, M., L. Goeyens, and E. Fahrbach (2000a), Intense nutrient removal in the remote area off Larsen Ice Shelf (Weddell Sea), *Polar Biol.*, *23*(2), 85–94.

Hoppema, M., M. H. C. Stoll, and H. J. W. de Baar (2000b), CO_2 in the Weddell Gyre and Antarctic Circumpolar Current: Austral autumn and early winter, *Mar. Chem.*, *72*(2), 203–220.

Hoppema, M., R. Middag, H. J. W. de Baar, E. Fahrbach, E. M. van Weerlee, and H. Thomas (2007), Whole season net community production in the Weddell Sea, *Polar Biol.*, *31*(1), 101–111.

Huang, K., H. Ducklow, M. Vernet, N. Cassar, and M. L. Bender (2012), Export production and its regulating factors in the West Antarctica Peninsula region of the Southern Ocean, *Global Biogeochem. Cycles*, *26*, GB2005, doi:10.1029/2010GB004028.

Jennings, J. C., L. I. Gordon, and D. M. Nelson (1984), Nutrient depletion indicates high primary productivity in the Weddell Sea.

Johnson, K. M., J. M. Sieburth, P. J. L. Williams, and L. Brandstrom (1987), Coulometric total carbon-dioxide analysis for marine studies: Automation and calibration, *Mar. Chem.*, *21*(2), 117–133.

Jones, E. M., D. C. E. Bakker, H. J. Venables, M. J. Whitehouse, R. E. Korb, and A. J. Watson (2010), Rapid changes in surface water carbonate chemistry during Antarctic sea ice melt, *Tellus, Ser. B*, *62*, 621–635.

Jonsson, B. F., S. C. Doney, J. Dunne, and M. Bender (2013), Evaluation of the Southern Ocean O_2/Ar-based NCP estimates in a model framework, *J. Geophys. Res. Biogeosci.*, *118*, 1–15, doi:10.1002/jgrg.20032.

Kaiser, J., M. K. Reuer, B. Barnett, and M. L. Bender (2005), Marine productivity estimates from continuous O_2/Ar ratio measurements by membrane inlet mass spectrometry, *Geophys. Res. Lett.*, *32*, L19605, doi:10.1029/2005GL023459.

Keeling, R. F. (1993), On the role of large bubbles in air-sea gas exchange and supersaturation in the ocean, *J. Mar. Res.*, *51*(2), 237–271.

Klunder, M. B., P. Laan, R. Middag, H. J. W. De Baar, and J. C. Van Ooijen (2011), Dissolved iron in the Southern Ocean (Atlantic sector), *Deep Sea Res., Part II*, *58*(25), 2678–2694.

Kortzinger, A., et al. (2008), Seasonal cycle of O_2 and pCO_2 in the central Labrador Sea: Atmospheric, biological, and physical implications, *Global Biogeochem. Cycles*, *22*, GB1014, doi:10.1029/2007GB003029.

Laubscher, R. K., R. Perissinotto, and C. D. McQuaid (1993), Phytoplankton production and biomass at frontal zones in the Atlantic sector of the Southern Ocean, *Polar Biol.*, *13*(7), 471–481.

Laws, E. A. (1991), Photosynthetic quotients, new production and net community production in the open ocean, *Deep Sea Res., Part A*, *38*(1), 143–167.

Liang, J. H., C. Deutsch, J. C. McWilliams, B. Baschek, P. P. Sullivan, and D. Chiba (2013), Parameterizing bubble-mediated air-sea gas exchange and its effect on ocean ventilation, *Global Biogeochem. Cycles*, *27*, 894–905, doi:10.1002/gbc.20080.

Loose, B., W. R. McGillis, P. Schlosser, D. Perovich, and T. Takahashi (2009), Effects of freezing, growth, and ice cover on gas transport processes in laboratory seawater experiments, *Geophys. Res. Lett.*, *36*, L05603, doi:10.1029/2008GL036318.

Lorbacher, K., D. Dommernget, P. P. Niiler, and A. Köhl (2006), Ocean mixed layer depth: A subsurface proxy of ocean–atmosphere variability, *J. Geophys. Res.*, *111*, C07010, doi:10.1029/2003JC002157.

Marinov, I., A. Gnanadesikan, J. R. Toggweiler, and J. L. Sarmiento (2006), The Southern Ocean biogeochemical divide, *Nature*, *441*(7096), 964–967.

Martinson, D. G., and D. C. McKee (2012), Transport of warm Upper Circumpolar Deep Water onto the western Antarctic Peninsula continental shelf, *Ocean Sci.*, *8*(4), 433.

McNeil, C. L., B. D. Johnson, and D. M. Farmer (1995), In situ measurement of dissolved nitrogen and oxygen in the ocean, *Deep Sea Res., Part I*, *42*(5), 819–826.

McNeil, C., D. Katz, R. Wanninkhof, and B. Johnson (2005), Continuous shipboard sampling of gas tension, oxygen and nitrogen, *Deep Sea Res., Part I*, *52*(9), 1767–1785.

Mehrbach, C., C. H. Culberso, J. E. Hawley, and R. M. Pytkowic (1973), Measurement of apparent dissociation constants of carbonic acid in seawater at atmospheric pressure, *Limnol. Oceanogr.*, *18*(6), 897–907.

Nicholson, D., S. Emerson, and C. C. Eriksen (2008), Net community production in the deep euphotic zone of the subtropical North Pacific gyre from glider surveys, *Limnol. Oceanogr.*, *53*(5), 2226.

Nicholson, D., S. Emerson, and C. C. Eriksen (2011), An inverse approach to estimate bubble-mediated air-sea gas flux from inert gas measurements, in *Proceedings on the 6th International Symposium on Gas Transfer at Water Surfaces*, pp. 223–237, Kyoto Univ. Press, Kyoto.

Orsi, A. H., T. Whitworth III, and W. D. Nowlin Jr. (1995), On the meridional extent and fronts of the Antarctic Circumpolar Current, *Deep Sea Res., Part I, 42*(5), 641–673.

Pierrot, D., E. Lewis, and D. W. R. Wallace (2006), MS Excel program developed for CO_2 system calculations, in *ORNL/CDIAC-105. Carbon Dioxide Information Analysis Center*, Oak Ridge Natl. Lab., U.S. Dep. of Energy, Oak Ridge, Tenn.

Planquette, H., R. M. Sherrell, S. Stammerjohn, and M. P. Field (2013), Particulate iron delivery to the water column of the Amundsen Sea, Antarctica, *Mar. Chem., 153*, 15–30.

Reuer, M. K., R. M. Sherrell, S. Stammerjohn, and M. P. Field (2007), New estimates of Southern Ocean biological production rates from O_2/Ar ratios and the triple isotope composition of O_2, *Deep Sea Res., Part I, 54*(6), 951–974.

Rohardt, G., E. Fahrbach, and A. Wisotzki (2011), Physical oceanography during POLARSTERN cruise ANT-XXVII/2, in *Alfred Wegener Institute, Helmholtz Center for Polar and Marine Research*, Pangaea, Bremerhaven.

Rubin, S. I., T. Takahashi, D. W. Chipman, and J. G. Goddard (1998), Primary productivity and nutrient utilization ratios in the Pacific sector of the Southern Ocean based on seasonal changes in seawater chemistry, *Deep Sea Res., Part I, 45*(8), 1211–1234.

Sarmiento, J. L., and N. Gruber (2006), *Ocean Biogeochemical Dynamics*, Princeton Univ. Press, Princeton.

Sarmiento, J. L., and J. R. Toggweiler (1984), A new model for the role of the oceans in determining atmospheric pCO$_2$, *Nature, 308*(5960), 621–624.

Sarmiento, J. L., N. Gruber, M. A. Brzezinski, and J. P. Dunne (2004), High-latitude controls of thermocline nutrients and low latitude biological productivity, *Nature, 427*(6969), 56–60.

Schlitzer, R. (2002), Carbon export fluxes in the Southern Ocean: Results from inverse modeling and comparison with satellite-based estimates, *Deep Sea Res., Part II, 49*(9–10), 1623–1644.

Schudlich, R., and S. Emerson (1996), Gas supersaturation in the surface ocean: The roles of heat flux, gas exchange, and bubbles, *Deep Sea Res., Part II, 43*(2), 569–589.

Sedwick, P. N., and G. R. DiTullio (1997), Regulation of algal blooms in Antarctic shelf waters by the release of iron from melting sea ice, *Geophys. Res. Lett., 24*(20), 2515–2518, doi:10.1029/97GL02596.

Shadwick, E. H., B. Tilbrook, N. Cassar, T. W. Trull, and S. R. Rintoul (2014), Summertime physical and biological controls on O_2 and CO_2 in the Australian sector of the Southern Ocean, *J. Mar. Syst., 147*, 21–28, doi:10.1016/j.jmarsys.2013.12.008.

Smith, W. O., and L. I. Gordon (1997), Hyperproductivity of the Ross Sea (Antarctica) polynya during austral spring, *Geophys. Res. Lett., 24*(3), 233–236.

Smith, W. O., and D. M. Nelson (1985), Phytoplankton bloom produced by a receding ice edge in the Ross Sea—Spatial coherence with the density field, *Science, 227*(4683), 163–166.

Sokolov, S. (2008), Chlorophyll blooms in the Antarctic Zone south of Australia and New Zealand in reference to the Antarctic Circumpolar Current fronts and sea ice forcing, *J. Geophys. Res., 113*, C03022, doi:10.1029/2007JC00.

Sokolov, S., and S. R. Rintoul (2007), On the relationship between fronts of the Antarctic Circumpolar Current and surface chlorophyll concentrations in the Southern Ocean, *J. Geophys. Res., 112*, C07030, doi:10.1029/2006JC004072.

Spreen, G., L. Kaleschke, and G. Heygster (2008), Sea ice remote sensing using AMSRE 89 GHz channels, *J. Geophys. Res., 113*, C02S03, doi:10.1029/2005JC003384.

Stanley, R. H. R., W. J. Jenkins, D. E. Lott, and S. C. Doney (2009), Noble gas constraints on air-sea gas exchange and bubble fluxes, *J. Geophys. Res., 114*, C11020, doi:10.1029/2009JC005396.

Sweeney, C. (2003), The annual cycle of surface CO_2 and O_2 in the Ross Sea: A model for gas exchange on the continental shelves of Antarctica, in *Biogeochemistry of the Ross Sea, Antarct. Res. Ser.*, vol. 78, edited by G. R. DiTullio and R. B. Dunbar, pp. 295–312, Washington, D. C.

Sweeney, C., E. Gloor, A. R. Jacobson, R. M. Key, G. McKinley, J. L. Sarmiento, and R. Wanninkhof (2007), Constraining global air-sea gas exchange for CO_2 with recent bomb C-14 measurements, *Global Biogeochem. Cycles, 21*, GB2015, doi:10.1029/2006GB0.

Takahashi, T., et al. (2002), Global sea-air CO_2 flux based on climatological surface ocean pCO$_2$, and seasonal biological and temperature effects, *Deep Sea Res., Part II, 49*(9–10), 1601–1622.

Takahashi, T., S. C. Sutherland, R. Wanninkhof, C. Sweeney, R. A. Feely, D. W. Chipman, B. Hales, G. Friederich, F. Chavez, and C. Sabine (2009), Climatological mean and decadal change in surface ocean pCO$_2$, and net sea-air CO_2 flux over the global oceans, *Deep Sea Res., Part II, 56*(8–10), 554–577.

Tortell, P. D., and M. C. Long (2009), Spatial and temporal variability of biogenic gases during the Southern Ocean spring bloom, *Geophys. Res. Lett., 36*, L01603, doi:10.1029/2008GL035819.

Tortell, P. D., C. Guéguen, M. C. Long, C. D. Payne, P. Lee, and G. R. DiTullio (2011), Spatial variability and temporal dynamics of surface water pCO$_2$, ΔO2/Ar and dimethylsulfide in the Ross Sea, Antarctica, *Deep Sea Res., Part I, 58*(3), 241–259.

Tortell, P. D., M. C. Long, C. D. Payne, A. C. Alderkamp, P. Dutrieux, and K. R. Arrigo (2012), Spatial distribution of pCO$_2$, ΔO_2/Ar and dimethylsulfide (DMS) in polynya waters and the sea ice zone of the Amundsen Sea, Antarctica, *Deep Sea Res., Part II, 71–76*, 77–93.

Tortell, P. D., E. C. Asher, H. Ducklow, J. A. L. Goldman, J. W. H. Dacey, J. J. Grzymski, J. N. Young, S. A. Kranz, K. S. Bernard, and F. M. M. Morel (2014), Metabolic balance of coastal Antarctic waters revealed by autonomous pCO$_2$ and ΔO_2/Ar measurements, *Geophys. Res. Lett., 41*, 6803–6810, doi:10.1002/2014GL061266.

Trull, T. W., S. G. Bray, S. J. Manganini, S. Honjo, and R. Francois (2001), Moored sediment trap measurements of carbon export in the Subantarctic and Polar Frontal Zones of the Southern Ocean, south of Australia, *J. Geophys. Res., 106*(C12), 31,489–31,509, doi:10.1029/2000JC000308.

Vagle, S., C. McNeil, and N. Steiner (2010), Upper ocean bubble measurements from the NE Pacific and estimates of their role in air-sea gas transfer of the weakly soluble gases nitrogen and oxygen, *J. Geophys. Res., 115*, C12054, doi:10.1029/2009JC005990.

Waters, K. J., and R. C. Smith (1992), Palmer LTER: A sampling grid for the Palmer LTER program, *Antarct. J. U. S., 27*(5), 236–239.

Weeding, B., and T. W. Trull (2014), Hourly oxygen and total gas tension measurements at the Southern Ocean Time Series site reveal winter ventilation and spring net community production, *J. Geophys. Res. Oceans, 119*, 348–358, doi:10.1002/2013JC009302.

Weiss, R. F. (1974), Carbon dioxide in water and seawater: The solubility of a non-ideal gas, *Mar. Chem., 2*(3), 203–215.